applied optics

Photonic Moiré lattice waveguide with a large slow light bandwidth and delay-bandwidth product

Ibrahim Nasidi,[1] Ran Hao,[2,*] Jun Chen,[2] Erping Li,[1] and ShangZhong Jin[2]

[1]College of Information Science and Electronic Engineering, Zhejiang University, Hangzhou 310027, China
[2]College of Optical and Electronic Technology, China Jiliang University, Hangzhou 310018, China
*Corresponding author: ran.hao@cjlu.edu.cn

Received 22 April 2022; revised 31 May 2022; accepted 12 June 2022; posted 14 June 2022; published 27 June 2022

We proposed an effective approach to enlarge the slow light bandwidth and normalized-delay-bandwidth product in an optimized moiré lattice-based photonic crystal waveguide that exhibits intrinsic mid-band characteristics. A flatband corresponding to a nearly constant group index of 34 over a wide bandwidth of 82 nm centered at 1550 nm with near-zero group velocity dispersion was achieved. A large normalized-delay-bandwidth product of 0.5712 with a relative dispersion of 0.114%/μm was obtained, which is a significant improvement if compared with previous results. Our results indicate that the photonic moiré lattice waveguide could advance slow light applications.

https://doi.org/10.1364/AO.462016

1. INTRODUCTION

The moiré lattice emerges upon superimposing two or more similar periodic structures with different lattice constants or rotation angles. Due to their unprecedented advantage in providing abundant optical properties at twist angles, the moiré lattice has attracted attention from the community. To date, moiré lattices have been extensively studied in enhancing nanophotonics components with great potential applications. Fu *et al*. [1] observed an optical soliton formation that is controlled by twist angle in a photonic moiré lattice for application in integrated light sources. Similarly, in photonic moiré lattices, localization and de-localization of light in a nonlinear crystal were observed for light pattern control [2] and light propagation/modulation due to optical interference [3,4]. Wu *et al*. [5] reported a plasmonic metamaterial for application in sensors. The moiré pattern has also been observed in graphene-based platforms that were used to realize superconductors [6] and mid-infrared photodetectors [7], which have shown significant improvement in light–matter interactions. However, the explorations of the moiré lattice with engineered dispersion effects have not been previously investigated, especially for slow light phenomena in photonic crystals that emphasize both strong dispersion and light–matter interactions. We envisioned photonic crystal based on a moiré lattice to be intuitively promising for slow light devices with improved performance.

Slow light has fascinated immense attention in the optical community because it is used for the delay and temporary storage of light and optical signal processing [8]. Slow light in the silicon photonic crystal waveguide (PhCW) with its compact size offers an approach to enhance light–matter interaction, which has been utilized in various applications such as sensing [9], microheaters [10], modulators [11], photodetectors [12], and nonlinear applications [13]. Among the silicon PhCW, two-dimensional (2D) PhCW is a robust platform for realizing slow light because of its ease of integration with on-chip devices. However, its performance has been limited by large group velocity dispersion (GVD) due to the realization of the slow light at the band edge. Recently, slow light performance in 2D PhCW was enhanced by integrating the PhCW with materials with large dispersion such as graphene [14,15], optical fluid [16], polymer substrate [17], and Kerr effect [18]. These approaches still have the effect of exciting large GVD, which limits the operational bandwidth.

In this paper, we propose a novel design of an all-dielectric photonic moiré lattice waveguide (PMLW) that facilitates slow light performance enhancement. Compared with conventional PhCW based on triangular and square lattices, the PMLW exhibits intrinsic mid-band slow light characteristics and more flexible control that allow sophisticated dispersion engineering and optimization. The proposed PMLW achieved an average group index (n_g) of 34, a bandwidth of 82 nm, near-zero GVD over the bandwidth, and a normalized delay-bandwidth product (NDBP) of 0.5712 with a relative dispersion of 0.114%/μm. Our design of wideband waveguide could find applications in practical slow light devices.

2. DESIGN METHOD

The moiré lattice is created by overlapping two similar 2D periodic square sublattices with either sublattice rotated by an

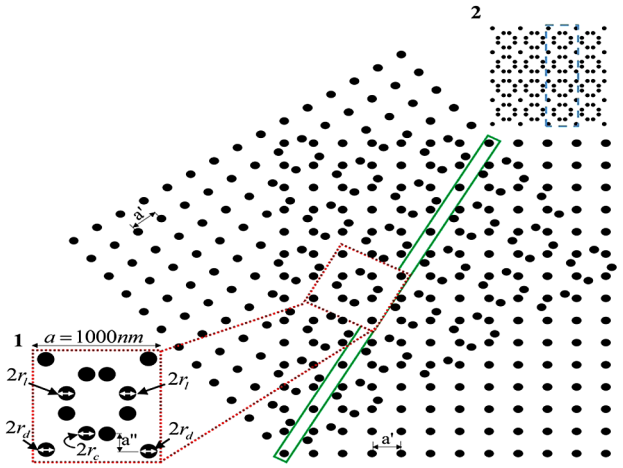

Fig. 1. Formation of the moiré lattice. The red dotted box shows a moiré cluster with 12 rods per unit cell, and the green solid box shows the region for the waveguide. Inset 1 shows a magnified moiré cluster with selected rods as indicated by the arrow. Inset 2 shows the sketch of the structure designed in MPB, and the blue dashed box shows the supercell used in PWE calculations.

angle θ. For a particular rotation angle θ, such that $\tan\theta = b/a$, where "a" and "b" belong to Pythagorean triples (a, b, c), the moiré lattice that emerges could be periodic or aperiodic. Figure 1 shows the formation of the moiré lattice. Two similar square sublattices each with periodicity $a' = 450$ nm and Pythagorean triples $(3, 4, 5)$ such that $\theta = \tan^{-1}(3/4) = 36.87^0$ were considered. Rotating either sublattice by $\theta = 36.87^0$ and overlaying both sublattices in one plane, a square periodic moiré lattice of periodicity $a = 1000$ nm appears with certain rods of the sublattices coinciding as depicted by the green solid box in Fig. 1. By separating and shifting one row of the coincident rods by $a'' = 201$ nm in $\pm y$ direction, a line defect is formed. The red dotted box (and inset 1 of Fig. 1) shows 12 dielectric rods per unit cell of the moiré lattice forming a moiré cluster (MC).

The 2D PMLW was designed with circular dielectric rods of $\varepsilon = 12$ and thickness $h = 220$ nm. Full three-dimensional (3D) simulation is required to precisely model the PMLW, but 3D simulation is computationally intensive. To balance the accuracy and effectiveness, the effective index method (EIM) and 2D simulation are employed together, where the 2D effective index replaces the actual 3D material refractive index so that the simulation can be performed in 2D with much less time but maintain almost the same accuracy as 3D simulation [19]. For transverse magnetic (TM) polarization, the dispersion band relation was analyzed using the plane wave expansion (PWE) method with the Massachusetts Institute of Technology (MIT) photonic bands (MPBs) package. The PWE method uses a 3D algorithm that uses periodic boundary conditions to compute definite frequency eigenstates and eigenmodes of a large supercell. The supercell is $a \times 20a$ in $x-y$ plane as depicted by the blue dashed box of inset 2 in Fig. 1. To improve accuracy and better reflect small changes in the structural parameters, 32×32 computational grid resolution, mesh size of 7, and tolerance decreased to 1×10^{-8} were used. The tolerance judges when convergence occurs, that is, when eigenvalues have a fractional change less than the tolerance between iterations.

3. RESULTS AND DISCUSSION

Before we explore the optical properties of the 2D photonic moiré lattice, let us discuss the bulk band structure of the moiré unit cell. It is worth mentioning that we deliberately chose $a' = 450$ nm sublattice periodicity to design the moiré lattice because it splits some bands in the band structure and lifts degenerate points, which opens up the bandgap. Figure 2(a) shows the photonic band structure of the moiré unit cell when all the rod radii are set to 0.078a. It can be seen that two positional bandgaps exist at the high normalized frequency with many folded bands at the low normalized frequency. The calculated bandgap width between bands 5 and 6 is $0.015(a/\lambda)$ (2.34%) while that of bands 6 and 7 is $0.042(a/\lambda)$ (5.84%). We chose to explore the guided mode between bands 6 and 7 because it has vanishing group velocity (v_g). The vanishing v_g could be attributed to flatbands in the vicinity of the bandgap frequency [see band 7 in Fig. 2(a)]. Moreover, degenerate points (bands) could be observed in the band structure at a low normalized frequency. The degenerate point could be explored to study the localization of light [20]. Therefore, the implication of having multiple rods per unit cell is that the dielectric contrast of the structure will be modified, which will result in a shift in the frequency position of photonic bandgaps and changes in the bandgap width [21], degenerate bands, and degenerate points.

To analyze the slow light performance of the structure, we set the radii of all the 12 dielectric rods to $0.078a$ and computed the dispersion band, n_g, bandwidth, GVD, and NDBP. Figure 2(b) shows the dispersion band with slow light region $0.7578(a/\lambda) - 0.7620(a/\lambda)$ for wave vector (k) range $0.238(2\pi/a) - 0.405(2\pi/a)$. This corresponds to $n_g = 38.6$ (within $\pm$ 10% average n_g) over 27.2 nm bandwidth (centered at 1550 nm) and NDBP = 0.215 as depicted by the black line with circles in Fig. 2(c). This result shows that our structure exhibits an intrinsic mid-band slow light characteristic. This is because our designed moiré lattice can be treated as a doubly

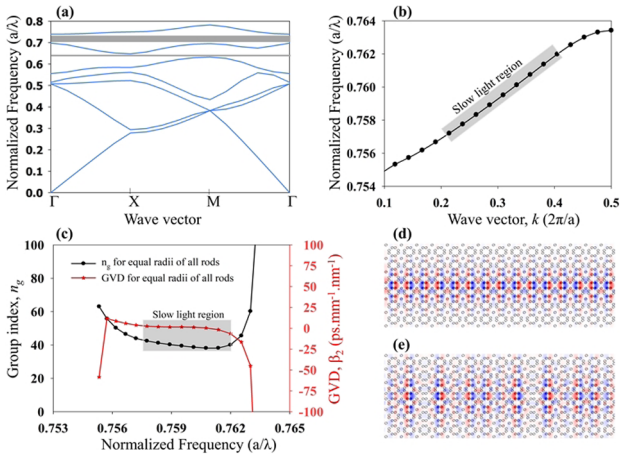

Fig. 2. (a) Bulk band structure for the photonic moiré unit cell with rod radii $0.078a$. The highlighted part indicates bandgap regions. (b) Dispersion band for the guided mode in the supercell for uniform rods radii of $0.078a$. (c) n_g and β_2 against normalized frequency for the dispersion band. (d) Field distribution at $k = 0.5(2\pi/a)$. (e) Field distribution at $k = 0.28(2\pi/a)$. The highlighted part in (b) and (c) indicates the slow light region.

resonant system that is made of two photonic crystal sublattices of slightly different resonant frequencies. The merging of the two sublattices created moiré lattices with rods that serve as scatterers, which appear closer to each other than in their sublattices, causing backward scattering at each moiré unit cell. The formation of the scatterers enhances the interaction control more precisely between the forward and the backscattered waves in a smaller space. The multiple scattering between these close scatterers allows incoherent interference. Therefore, the large flat mid-band slow light occurs as a consequence of incoherent interference due to the breakdown of translation symmetry resulting from the merging of the two sublattices [20,22,23]. Moreover, by having slow light at mid-band, dispersion and backscattering loss will have less effect [24]. The GVD was calculated numerically from the $\omega-k$ relation defined by the GVD parameter (β_2) as $\beta_2 = d^2k/d\omega^2$. A near-zero β_2 can be seen over the slow light bandwidth as shown by the red star line in Fig. 2(c). The β_2 increases (toward negative) outside the near-zero frequency range, which signifies the fast light region. Despite the interesting and promising capabilities observed so far, that is, $n_g = 38.6$, bandwidth = 27.2 nm, and NDBP = 0.215, the performance is unsatisfactory. Therefore, a systematic approach that involves extensive parameter optimization is required to enhance the performance.

The field distributions of the guided mode can be explored to tailor the dispersion properties of the PMLW. Figures 2(d) and 2(e) show the field distribution for guided modes at $k = 0.5(2\pi/a)$ and $k = 0.28(2\pi/a)$, respectively. The mode can be seen to be confined within the waveguide core at $k = 0.5(2\pi/a)$. In the slow light region, at $k = 0.28(2\pi/a)$, the mode can be seen to be dispersed into the PMLW structure and concentrated on the dielectric rods, which highlight that the properties of the mode in the slow light region depend on the PMLW structural parameters [25].

The goal of slow light devices is to achieve slow light operation over the widest possible bandwidth, relatively high n_g, large NDBP, low dispersion, and low propagation loss. The intrinsic mid-band property of our structure assures low dispersion and less backscattering loss [24]. To minimize propagation loss, we limit the n_g below 40 because n_g above 40 in PhCW leads to an exponential rise in loss [26], and the loss per unit time decreases within $n_g = 30-40$ [27]. Hence, we enlarge the NDBP by widening the bandwidth, taking advantage of the mid-band slow light characteristic.

Dispersion engineering and optimization were carried out to discern the rod parameters that positively influence the band and widen the bandwidth, respectively. All the 12 dielectric rod parameters in the MC merit study. For brevity, and because some parameters offer similar influence, a few selected rods labeled r_c, r_l, and r_d as indicated in inset 1 of Fig. 1 are reported here. The strategy is to carefully fine-tune the selected parameters such that the dispersion band slope is as constant as possible over a wide wave vector range, which simultaneously expands the flatband frequency region. This was achieved by increasing r_c and r_l then decreasing r_d. The process was carried out geometrically; that is, previously optimized rods are kept at the optimized value in subsequent steps. A value is considered optimized when further variation (that is, increase or decrease) decreases the bandwidth.

Figure 3(a) shows the influence of r_c variation on the band. An increase in r_c could be seen moving down the band to the low normalized frequency in the entire wave vector k range and increasing the slope steepness. This indicates that an increase in r_c changes resonant frequency and control band shape. This is evident in Fig. 3(b), which shows the n_g against normalized frequency plots for increase $r_c (0.078a \le r_c \le 0.0833a)$ with $r_l = r_d = 0.078a$ and the remaining rods also kept at $0.078a$ (remaining rods refer to those five rods not among the selected. They are denoted as r' and will, henceforth, be referred to as such). By increasing r_c, the curve was decently tuned and flattened, thereby increasing n_g and bandwidth. At $r_c = 0.0833a$, $n_g = 41$, bandwidth = 37.14 nm, and NDBP = 0.314. When $r_c > 0.0833a$, the bandwidth decreases. Figure 3(c) depicts the behavior of the band when r_l is varied. Increasing r_l causes significant band shift to the low normalized frequency near the small wave vector ($k < 0.1$) but minor band shift at the large wave vector. This highlights that r_l influences the left band edge. To confirm this assertion, the n_g against a normalized frequency curve is plotted. Figure 3(d) shows an increase in $r_l (0.078a \le r_l \le 0.0825a)$ with $r_c = 0.0833a$, $r_d = r' = 0.078a$. By increasing r_l, the n_g curve shows a significant shift at the low normalized frequency edge and a slight shift at the high normalized frequency edge. This extends the frequency range from the left edge and, thus, increases the bandwidth. At $r_l = 0.0815a$, bandwidth = 47.9 nm, $n_g = 39.6$, and NDBP = 0.39. When $r_l > 0.0815a$, the bandwidth decreases. Figure 3(e) depicts the behavior of the band when r_d is varied. The decrease in r_d shows a significant band shift to the high normalized frequency at large wave vectors near $k \ge 0.4$ with no

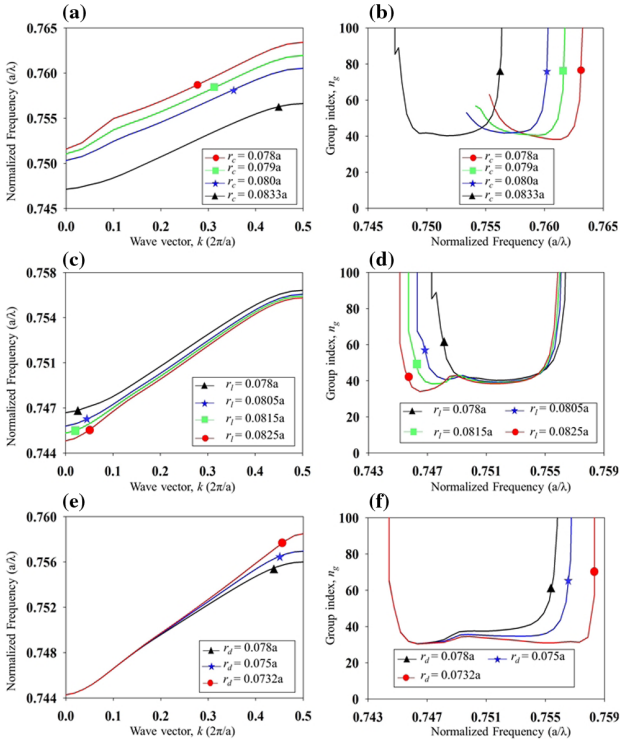

Fig. 3. Dispersion engineering and optimization for selected dielectric rods. Normalized frequency against wave vector for (a) r_c variation, (c) r_l variation, (e) r_d variation. n_g against normalized frequency curves for (b) increasing r_c, (d) increasing r_l, (f) decreasing r_d.

Table 1. Details of Optimization with Corresponding Group Index, Bandwidth, and NDBP at Each Step

Steps	n_g	Bandwidth (nm)	NDBP
Uniform rod radii	38.6	27.2	0.215
$r_c = 0.0833a$	41	37.14	0.3142
$r_l = 0.0815a$	39.6	47.9	0.39
$r_d = 0.0732a$	34	82	0.5712

band shift at small wave vectors. This shows that r_d influences the right band edge. Figure 3(f) presents the result of decreasing r_d from $0.078a$ to $0.0732a$ with $r_c = 0.0833a$, $r_l = 0.0815a$, and $r' = 0.078a$. Decreasing r_d significantly shifts and extends the curve in the high normalized frequency edge with no shift in the low normalized frequency edge. This extends the frequency range from the right edge, which further increases the bandwidth. At $r_d = 0.0732a$, bandwidth = 82 nm, $n_g = 34$, and NDBP = 0.5712. When $r_d < 0.0732a$, the bandwidth decreases. Table 1 presents a detailed summary of the optimization with the corresponding slow light figure of merits (FOMs) at each stage. It could be seen that the bandwidth and the NDBP increase after each optimization step. The mechanism for widening the bandwidth can be explained from the perspective of double spatial resonance that allows for the creation of a moiré lattice with 12 rods per unit cell. This large number of rods in the moiré unit cell gives enormous flexibility to control the dispersion band by exploiting the vast degree of freedom to create multiple resonances [28]. The change in rod radii causes changes in the effective index, which causes various resonances. We carefully balance these resonances through sweeping to create slow light that covers a considerable frequency range as seen in Fig. 3.

Figure 4 compares the slow light performance "before" and "after" the optimization. The black and red solid line shows the n_g and GVD curves, respectively, for optimal values. The optimal values are the values that give the widest bandwidth of 82 nm and largest NDBP of 0.5712 "after" the optimization. They are $r_c = 0.0833a$, $r_l = 0.0815a$, $r_d = 0.0732a$, and $r' = 0.078a$. The black and red dashed line illustrates the n_g and GVD curves "before" optimization, that is, when all the rods in MC have the same radii of 0.078a, which gives a bandwidth = 27.2 nm, $n_g = 38.6$, and NDBP = 0.215. Comparison of the bandwidth between "before" and "after" the optimization

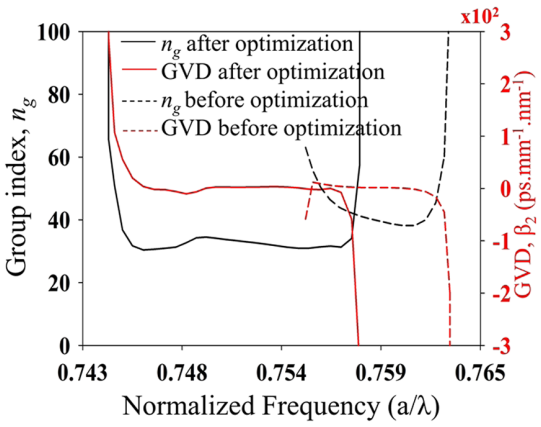

Fig. 4. Slow light performance comparison of n_g and GVD before and after optimization.

Table 2. Group Index, Bandwidth, and NDBP Comparison between Current Work and Conventional Photonic Crystal Waveguides

References	n_g	Bandwidth (nm)	NDBP	Relative Dispersion (%/μm)
Current work	34	82	0.5712	0.114
[16]	20.1	36.8	0.469	0.75
[30]	80	8.6	0.44	0.12
[31]	13.6	58.4	0.502	0.6
[32]	37	17.7	0.47	–
[34]	28	26.5	0.48	–

gives a 300% increase in bandwidth. Our slow light FOM, that is, n_g, bandwidth, and relative dispersion, is better if compared with previous results [16,29–34] as detailed in Table 2. Our NDBP value is 1 order of magnitude larger than [18], and 1.19 and 1.14 times larger than [34] and [31], respectively. From the GVD β_2 curves, a near-zero dispersion over the bandwidth in both cases could be observed. Extreme β_2 can be seen outside the near-zero dispersion range, which shows dispersion flattening and dispersion compensation capabilities of the waveguide [35].

4. TIME DOMAIN ANALYSIS

To verify the accuracy of PWE results, a 2D FDTD simulation was performed with perfectly matched layers absorbing boundary conditions around the structure. The wide bandwidth of 82 nm from $0.7452(a/\lambda)$ to $0.757877(a/\lambda)$ and corresponding average $n_g = 34$ were obtained using the optimal values. Then a structure of length $20a$ was designed with these values. A Gaussian pulse source with center frequency at $0.749822(a/\lambda)$ and frequency width $0.012677(a/\lambda)$ was used. Input and output monitors were stationed at a distance $1a$ from the boundary on both sides of the waveguide; thus, the propagation length $L = 18a$. Figure 5 shows normalized field intensity detected by the input and output monitors placed along the waveguide. The pulse peak intensity for the input and output monitors was detected at $32.675(a/c)$ and $632.484(a/c)$, respectively. Therefore, the time delay $\Delta t = 599.81(a/c)$. The n_g calculated using $n_g = c\Delta t/L$ is 33.3, which is in good agreement with n_g obtained using PWE calculations.

The propagation loss in the waveguide was computed using the peak optical energies detected by the two monitors stationed

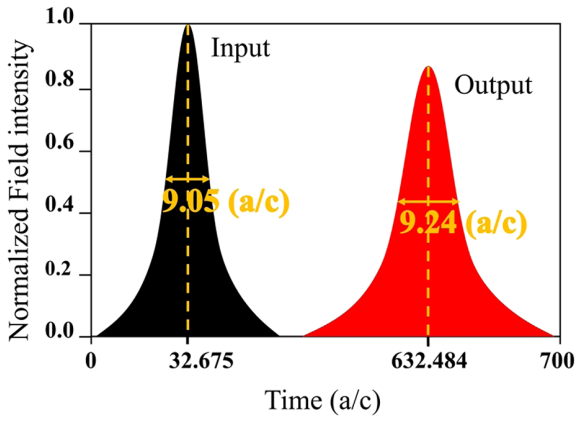

Fig. 5. Time domain pulse propagation.

at the input and output along the propagation direction [14]. The ratio of the output monitor peak energy to the input monitor peak energy is computed to be −13.35 dB. This low loss confirms our earlier assertion of dependence on loss on n_g.

The dispersion was computed by calculating pulse broadening using full width at half-maximum (FWHM). The FWHM at input and output monitors are $9.05(a/c)$ and $9.24(a/c)$, respectively. Therefore, the pulse broadening is $0.19(a/c)$. The relative pulse broadening is only 2.09% equivalent to 0.114%/μm, which is very low if compared with previous results [16,17,30,31,36]. Therefore, the pulse broadened by 0.63 fs over 18 μm propagation length and 82 nm bandwidth. This implies that the pulse broadened by 0.00043 fs per bandwidth per micrometer propagation length. Hence, the GVD parameter β_2 is 0.00043 $\mathrm{fs}\cdot\mathrm{nm}^{-1}\cdot\mu\mathrm{m}^{-1}$, which is a near-zero value and confirms the minimal dispersion achieved from the dispersion relation. This small dispersion is directly attributed to the intrinsic mid-band characteristic of the waveguide.

5. CONCLUSION

In this study, a PhCW in a moiré lattice was designed for slow light performance enhancement. Our designed structure creates mid-band slow light, which shows inherent low dispersion characteristics. We leveraged the mid-band property to enlarge bandwidth by 300% through systematic optimization. Ultrawide bandwidth of 82 nm, near-zero β_2 over the bandwidth, nearly constant n_g of 34, and NDBP of 0.5712 were achieved. The β_2 obtained from dispersion relation and FDTD matches very well. A relative dispersion of 0.114%/μm was obtained. Our novel design fulfills conditions for new photonic crystal lattices because it supports optical guided mode due to bandgap, it surpasses conventional lattices in terms of the slow light FOM being considered, that is, the NDBP, and the minimum dimensions that give good performance are not below the size attainable by state-of-the-art electron beam lithography technology. Therefore, the large NDBP and low dispersion would cause PhCW in a moiré lattice to have great potential for realistic slow light devices for buffering and pulse shaping.

Funding. National Natural Science Foundation of China (61575174, 61975182).

Acknowledgment. Ibrahim Nasidi is grateful to the Chinese government for the scholarship.

Disclosures. The authors declare no conflicts of interest.

Data availability. Data underlying the results presented in this paper are not publicly available at this time but may be obtained from the authors upon reasonable request.

REFERENCES

1. Q. Fu, P. Wang, C. Huang, Y. V. Kartashov, L. Torner, V. V. Konotop, and F. Ye, "Optical soliton formation controlled by angle twisting in photonic moiré lattices," Nat. Photonics **14**, 663–668 (2020).
2. P. Wang, Y. Zheng, X. Chen, C. Huang, Y. V. Kartashov, L. Torner, V. V. Konotop, and F. Ye, "Localization and delocalization of light in photonic moiré lattices," Nature **577**, 42–46 (2020).
3. C. Shang, C. Lu, S. Tang, Y. Gao, and Z. Wen, "Generation of gradient photonic moiré lattice fields," Opt. Express **29**, 29116–29127 (2021).
4. T. H. Talukdar, A. Hardison, and J. D. Ryckman, "Twistoptics in 1D: Silicon moiré photonic crystals," in *IEEE 17th International Conference on Group IV Photonics (GFP)* (IEEE, 2021), pp. 1–2.
5. Z. Wu and Y. Zheng, "Moiré chiral metamaterials," Adv. Opt. Mater. **5**, 1700034 (2017).
6. Y. Cao, V. Fatemi, S. Fang, K. Watanabe, T. Taniguchi, E. Kaxiras, and P. Jarillo-Herrero, "Unconventional superconductivity in magic-angle graphene superlattices," Nature **556**, 43–50 (2018).
7. B. Deng, C. Ma, Q. Wang, S. Yuan, K. Watanabe, T. Taniguchi, F. Zhang, and F. Xia, "Strong mid-infrared photoresponse in small-twist-angle bilayer graphene," Nat. Photonics **14**, 549–553 (2020).
8. B. Corcoran, C. Monat, C. Grillet, D. J. Moss, B. J. Eggleton, T. P. White, L. O'Faolain, and T. F. Krauss, "Green light emission in silicon through slow-light enhanced third-harmonic generation in photonic-crystal waveguides," Nat. Photonics **3**, 206–210 (2009).
9. L. Torrijos-Morán, A. Griol, and J. García-Rupérez, "Slow light bimodal interferometry in one-dimensional photonic crystal waveguides," Light Sci. Appl. **10**, 16 (2021).
10. S. Yan, X. Zhu, L. H. Frandsen, S. Xiao, N. A. Mortensen, J. Dong, and Y. Ding, "Slow-light-enhanced energy efficiency for graphene microheaters on silicon photonic crystal waveguides," Nat. Commun. **8**, 14411 (2017).
11. Y. Ma, B. Dong, B. Li, J. Wei, Y. Chang, and C. Lee, "Mid-infrared slow light engineered one-dimensional grating waveguide," *International Conference on Optical MEMS and Nanophotonics (OMN)*, July 2018.
12. Y. Ma, B. Dong, J. Wei, Y. Chang, L. Huang, K. W. Ang, and C. Lee, "High-responsivity mid-infrared black phosphorus slow light waveguide photodetector," Adv. Opt. Mater. **8**, 2000337 (2020).
13. Y. Ma, B. Dong, B. Li, K.-W. Ang, and C. Lee, "Dispersion engineering and thermo-optic tuning in mid-infrared photonic crystal slow light waveguides on silicon-on-insulator," Opt. Lett. **43**, 5504–5507 (2018).
14. R. Hao, X. L. Peng, E. P. Li, Y. Xu, J. M. Jin, X. M. Zhang, and H. S. Chen, "Improved slow light capacity in graphene-based waveguide," Sci. Rep. **5**, 15335 (2015).
15. X. Guo, X. Wu, H. Cui, F. Yang, and J. Zhou, "Slow light performance enhancement of graphene-based photonic crystal waveguide," Phys. Lett. A **383**, 1983–1987 (2019).
16. M. Pourmand, A. Karimkhani, and F. Nazari, "Wideband and low-dispersion engineered slow light using liquid infiltration of a modified photonic crystal waveguide," Appl. Opt. **55**, 10060–10066 (2016).
17. H. Wu, S. Han, F. Li, and Z. Yang, "Slow light with high normalized delay-bandwidth product in organic photonic crystal coupled-cavity waveguide," Appl. Opt. **59**, 642–647 (2020).
18. T. Daghooghi, M. Soroosh, and K. Ansari-Asl, "Slow light in ultracompact photonic crystal decoder," Appl. Opt. **58**, 2050–2057 (2019).
19. S. A. Schulz, A. H. K. Park, I. De Leon, J. Upham, and R. W. Boyd, "Beyond the effective index method: Improved accuracy for 2D simulations of photonic crystal waveguides," J. Opt. **17**, 075006 (2015).
20. G. Alagappan and C. E. Png, "Localization of waves in merged lattices," Sci. Rep. **6**, 31620 (2016).
21. H. A. Gómez-Urrea, M. C. Ospina-Medina, J. D. Correa-Abad, M. E. Mora-Ramos, and F. J. Caro-Lopera, "Tunable band structure in 2D Bravais–moiré photonic crystal lattices," Opt. Commun. **459**, 125081 (2020).
22. G. Tarnopolsky, A. J. Kruchkov, and A. Vishwanath, "Origin of magic angles in twisted bilayer graphene," Phys. Rev. Lett. **122**, 106405 (2019).
23. R. Bistritzer and A. H. MacDonald, "Moiré bands in twisted double-layer graphene," Proc. Natl. Acad. Sci. USA **108**, 12233–12237 (2011).
24. T. F. Krauss, "Slow light in photonic crystal waveguides," J. Phys. D **40**, 2666–2670 (2007).
25. L. H. Frandsen, A. V. Lavrinenko, J. Fagen-Pedersen, and P. I. Borel, "Photonic crystal waveguides with semi-slow light and tailored dispersion properties," Opt. Express **14**, 9444–9450 (2006).
26. L. O'Faolain, S. A. Schulz, D. M. Beggs, T. P. White, M. Spasenović, L. Kuipers, F. Morichetti, A. Melloni, S. Mazoyer, J. P. Hugonin, P. Lalanne, and T. F. Krauss, "Loss engineered slow light waveguides," Opt. Express **18**, 27627–27638 (2010).

27. T. F. Krauss, "Coupling and propagation losses in slow light (ng->100) photonic crystal waveguides," Proc. SPIE **7226**, 72260V (2009).
28. M. Martí-Sabaté and D. Torrent, "Dipolar localization of waves in twisted phononic crystal plates," Phys. Rev. Appl. **15**, L011001 (2021).
29. J. Pan, M. Fu, W. Yi, X. Wang, J. Liu, M. Zhu, J. Qi, S. Yin, G. Huang, S. Zhu, X. Chen, W. Tang, J. Liao, H. Yang, and X. Li, "Improving low-dispersion bandwidth of the silicon photonic crystal waveguides for ultrafast integrated photonics," Photonics **8**, 105 (2021).
30. X. Han, T. Wang, T. Jian, B. Liu, B. Wang, Y. He, and Y. Zhu, "Slow light with large group index–bandwidth product in ellipse-hole photonic crystal waveguides," Appl. Opt. **54**, 1543–1547 (2015).
31. F. Kuang, F. Li, Z. Yang, and H. Wu, "Wideband slow light in a line-defect annular photonic-crystal waveguide," Curr. Opt. Photon. **3**, 438–444 (2019).
32. Y. Lai, M. S. Mohamed, B. Gao, M. Minkov, R. W. Boyd, V. Savona, R. Houdré, and A. Badolato, "Ultra-wide-band structural slow light," Sci. Rep. **8**, 14811 (2018).
33. R. Hao, G. Ye, J. Jiao, and E. Li, "Increasing the bandwidth of slow light in fishbone-like grating waveguides," Photon. Res. **7**, 240–245 (2019).
34. S. Elshahat, K. Khan, A. Yadav, L. Bibbò, and Z. Ouyang, "Slow-light transmission with high group index and large normalized delay bandwidth product through successive defect rods on intrinsic photonic crystal waveguide," Opt. Commun. **418**, 73–79 (2018).
35. R. Hao, E. Cassan, H. Kurt, X. Le Roux, D. Marris-Morini, L. Vivien, H. Wu, Z. Zhou, and X. Zhang, "Novel slow light waveguide with controllable delay-bandwidth product and ultra-low dispersion," Opt. Express **18**, 5942–5950 (2010).
36. I. Abood, S. Elshahat, K. Khan, L. Bibbò, A. Yadav, and Z. Ouyang, "Slow light with high normalized delay-bandwidth product in low-dispersion photonic-crystal coupled-cavity waveguide," Opt. Commun. **439**, 181–186 (2019).